Origin of Zenneck-like waves excited by optical nanoantennas in non-plasmonic transition metals

Juemin Yi, Fernando de León-Pérez, Aurélien Cuche, Eloïse Devaux, Cyriaque Genet, Luis Martín-Moreno, Thomas W. Ebbesen

Research Article | Vol. 30, No. 19 / 12 Sep 2022 / Optics Express 34984
Optics EXPRESS

Origin of Zenneck-like waves excited by optical nanoantennas in non-plasmonic transition metals

JUEMIN YI,[1,2,*] FERNANDO DE LEÓN-PÉREZ,[3,6] AURÉLIEN CUCHE,[4] ELOÏSE DEVAUX,[1] CYRIAQUE GENET,[1,7] LUIS MARTÍN-MORENO,[5,8] AND THOMAS W. EBBESEN[1]

[1]*University of Strasbourg, CNRS, ISIS and icFRC, F- 67000 Strasbourg, France*
[2]*Suzhou Institute of Nano-Tech and Nano-Bionics, Chinese Academy of Sciences, Suzhou 215123, China*
[3]*Centro Universitario de la Defensa de Zaragoza, Ctra. de Huesca s/n, CP 50090, Zaragoza, Spain*
[4]*CEMES, University of Toulouse and CNRS (UPR 8011), 29 rue Jeanne Marvig, BP 94347, 31055 Toulouse, France*
[5]*Instituto de Nanociencia y Materiales de Aragón (INMA) and Departamento de Física de la Materia Condensada, CSIC-Universidad de Zaragoza, E- 50009 Zaragoza, Spain*
[6]*fdlp@unizar.es*
[7]*genet@unistra.fr*
[8]*lmm@unizar.es*
[*]*jmyi2020@sinano.ac.cn*

Abstract: The scattering properties of metallic optical antennas are typically examined through the lens of their plasmonic resonances. However, non-plasmonic transition metals also sustain surface waves in the visible. We experimentally investigate in this work the far-field diffraction properties of apertured optical antennas milled on non-plasmonic W films and compare the results with plasmonic references in Ag and Au. The polarization-dependent diffraction patterns and the leakage signal emerging from apertured antennas in both kinds of metals are recorded and analyzed. This thorough comparison with surface plasmon waves reveals that surface waves are launched on W and that they have the common abilities to confine the visible light at metal-dielectric interfaces offering the possibility to tailor the far-field emission. The results have been analyzed through theoretical models accounting for the propagation of a long range surface mode launched by subwavelength apertures, that is scattered in free space by the antenna. This surface mode on W can be qualitatively described as an analogy in the visible of the Zenneck wave in the radio regime. The nature of the new surface waves have been elucidated from a careful analysis of the asymptotic expansion of the electromagnetic propagators, which provides a convenient representation for explaining the Zenneck-like character of the excited waves and opens new ways to fundamental studies of surface waves at the nanoscale beyond plasmonics.

1. Introduction

The study of electromagnetic surface waves dates back to the last decade of the 19^{th} century when the radio waves were discovered by Hertz. In the context of rapid development of radio-wave technology, Zenneck and Sommerfeld were the first to predict theoretically the existence of surface waves (SW) generated by an infinitesimal vertical Hertzian dipole over a lossy dielectric medium (later named as Zenneck-Sommerfeld surface wave) [1,2]. Despite the discovery that the long range radio transmission originates from reflection on the ionosphere, the interest in the fundamental question of SW has remained high, and quite in-depth researches have taken place [3–5].

Taking advantage of the developments in nanofabrication during the two last decades, the concept of surface wave has been expanded to the visible range with the emergence of the

#467692 https://doi.org/10.1364/OE.467692
Journal © 2022 Received 17 Jun 2022; revised 18 Aug 2022; accepted 20 Aug 2022; published 9 Sep 2022

Optics EXPRESS

plasmonics field of research, which is dedicated to the study of propagating longitudinal electromagnetic (EM) waves at metal-dielectric interface [6]. The ability of these surface plasmons (SPs) to confine, enhance and propagate the EM field at two dimensions (2D) has triggered a strong interest in the NanoOptics community. As a consequence, a large variety of new optical phenomena have been observed such as enhanced Raman scattering [7,8], extraordinary optical transmission (EOT) [9,10], light beaming [11], nano-lasers [12,13] or optical trapping in the near field [14,15].

The similarity between other surface waves in the radio and visible frequency regimes (e.g. Norton, quasi-cylindrical and Zenneck-like waves) has been discussed previously [16–25]. Along with SP modes, the propagative properties of all these SW have been studied either experimentally or theoretically both in the near and far field. These works demonstrated that, even in a plasmonic metal, the dominant SP contribution goes along with other kinds of SW. SP waves at optical frequencies dominate over other SW on a broad but limited range of distances that extend from a fraction of the free-space wavelength to several times the propagation length [16–21,26]. Surprisingly, the contribution of SW on non-plasmonic metals leads to similar spectral features on optical antennas as observed for plasmonic systems. This more complete picture allowed notably to refine the understanding of the spectrally-dependent EOT mechanism, even on non-plasmonic W films [27–30]. In these previous works, it is mostly assumed that Zenneck waves are excited, but the precise nature of SW in W has not been established so far. Moreover, while some near-field mechanisms attributed to some of these SW have been already discussed, their use to tailor the far field emission has not been investigated yet.

The scattering properties of plasmonic dipolar antennas like nanospheres, nanorods or circular nanopads have been extensively studied and described in the literature [31–33]. In the same way, single holes in an opaque metallic film, which can be approximately described as reciprocal Babinet structures of circular nanopads [34], have been at the focus of numerous studies [21,35–40]. A thorough theoretical and experimental investigation of their far-field emission has been performed [41]. This work has somehow closed an old debate about the scattering of subwavelength holes by highlighting the two contributions responsible for the polarization- and size-dependent response of such apertures. Indeed, the far-field emission from a hole is driven by the field distribution associated to the waveguide mode inside the aperture (modulated by the size of the hole), and by the angular density of available EM states at the output. In the case of a metallic film with a SP resonance at a given wavelength, there is a depletion of the available photonic modes due to the excitation of the SP wave for wavevectors with a high planar component ($k_{||}$). If such subwavelength holes are arranged in hole arrays with large lattice spacing, the angular dependence of the integrated power can be straightforwardly measured and computed by looking at the discrete diffraction angles determined by higher diffraction orders, achieving better signal to noise ratio than in single-hole experiments [42].

In this paper, we focus on the far-field scattering response of several kinds of apertured optical antennas milled in a non-plasmonic metal in the visible. Tungsten (W) has been chosen because of the sign inversion of the real part of the metal permittivity, $\mathrm{Re}(\epsilon_m)$, which turns to be dielectric on a restricted domain of wavelength in the 240-920 nm spectral window, with $\mathrm{Re}(\epsilon_m)>0$, and cannot support SPs at the W/air interface. This is why W has already be at the focus of earlier studies aiming at unveil the EOT mechanism in hole arrays, where resonant peaks, similar to those observed in plasmonic metals but with lower intensities, have been reported [27–30]. It would therefore be worth to compare a non-plasmonic metallic film designed with such subwavelength dipolar apertured antenna with a plasmonic reference. The far-field diffraction patterns and the leakage signal emerging from a single dipolar apertured antenna or from more complex hole-grooves geometries are recorded and compared to either Ag or Au benchmarks supporting SP modes in the visible. In section 2, we identify the main scattering mechanisms for the far-field radiation of single holes and their relation to surface waves excited at both kind of metals, while

Optics EXPRESS

Sec. 3. describes interference effects in hole-grooves geometries. Experimental results are interpreted with the help of the coupled-mode method (CMM) [10]. The nature of surface waves and their contribution to the interference patterns reported in Sec. 3. are theoretically investigated by means of the asymptotic expansion of the propagators responsible for the electromagnetic interaction [3,19,21,43].

One could also mention recent results that showed the formation of periodical nanostructures on W surface by femtosecond laser technique [44,45], and significant field enhancement from W nanostructures [46]. In addition, tailoring of the thermal emission by the mean of bull's eye (BE) antenna in the infrared range has been reported [47]. These former studies give a hint that surface waves on W surfaces can be used to design optical antennas in the visible range following simple rules [48]. This point is discussed in Sec. 3.

2. Excitation of surface waves by a single aperture

We prepared single subwavelength circular holes by focused ion beam (FIB) lithography. These dipolar apertured antennas were milled through a 400 nm (h) thick W and Ag films sputtered on classical glass cover slides (thickness 1 mm). The thickness h=400 nm, which is much larger than twice the skin depth, is sufficient to ensure a total opacity of the films. In order to record the far-field electromagnetic field radiation, the samples were positioned and carefully aligned in the xy plane of our high stability homemade goniometer (see Fig. 1(a)) with silica glass substrate on the illumination side. Under weakly focused (10X, numerical aperture NA=0.3) and linearly polarized excitation at λ=660 nm, the transmitted far-field diffraction pattern are recorded by scanning in the xz plane a multimode optical fiber coupled to a spectrometer (from -60° to +30°) [41]. Diffraction patterns are recorded for p-polarization and s-polarization with the incident electric field respectively along the x-axis and the y-axis.

Figure 1(c) shows the experimental diffraction patterns of single holes (SHs) with a diameter d=350 nm in W and Ag films as a function of the incident polarization. The angular diffraction patterns are normalized by the intensity measured at direct transmission (θ = 0°). We know from our previous work that the presence of the substrate on the incident side has no incidence on the normalized diffraction patterns [41]. One can observe that, for each polarization, the measured diffraction patterns of SHs in Ag and W are virtually equal. These observations can be extended to the full range of hole sizes, leading to the three diffraction regimes ($I_S(\theta)<I_P(\theta)$ for $d<\lambda$ $I_S(\theta)=I_P(\theta)$ for $d \sim \lambda$, and $I_S(\theta)>I_P(\theta)$) for $d>\lambda$) that were previously identified in the case of Ag, see Supplement 1, Sec. 1.A. The main quantitative difference between small dipolar SHs in W and Ag films lies in the transmission intensity. Figure 1(d) reveals that the intensity along the optical axis, I(0°), of the smallest SHs (d=220 nm) is more than 10 times weaker for the W film than for the Ag film. In the evanescent transmission regime, for hole sizes below the cutoff diameter (d_c), intrinsic losses in the metal play a major role. Since the dissipation is related to the imaginary part of the permittivity, the differences observed in Fig. 1(d) can be explained by the difference between Im(ϵ_{Ag})=0.99 and Im(ϵ_W)=25.8 at λ=660 nm along with a deeper skin depth in W than in Ag (δ_{Ag}=25 nm and δ_W=49 nm). On the other hand, the transmission intensities for large holes in the two metals are the same, indicating that the propagation through the hole can be regarded as a waveguide process without energy loss. Interestingly, the slope of the semi-logarithmic plots in Fig. 1(d) reveals that the cutoff diameter d_c at λ=660 nm for the W film ($d_c \sim$ 300 nm) is slightly smaller than for the Ag one ($d_c \sim$ 400 nm).

Experimental trends in Fig. 1 can be explained with the analytical CMM approach outlined in Ref. [41]. Simple analytical expressions (represented with solid lines in Fig. 1) can be derived assuming that only the fundamental TE_{11} mode is excited inside the hole. Such expressions are given in Supplement 1 Sec. 2.A for the sake of completeness. In order to gain physical insight, calculated values for Ag and W are compared with those for an ideal perfect electric conductor (PEC) in Fig. 1(c). We find that, while the radiation pattern for *s*-polarization is

Optics EXPRESS

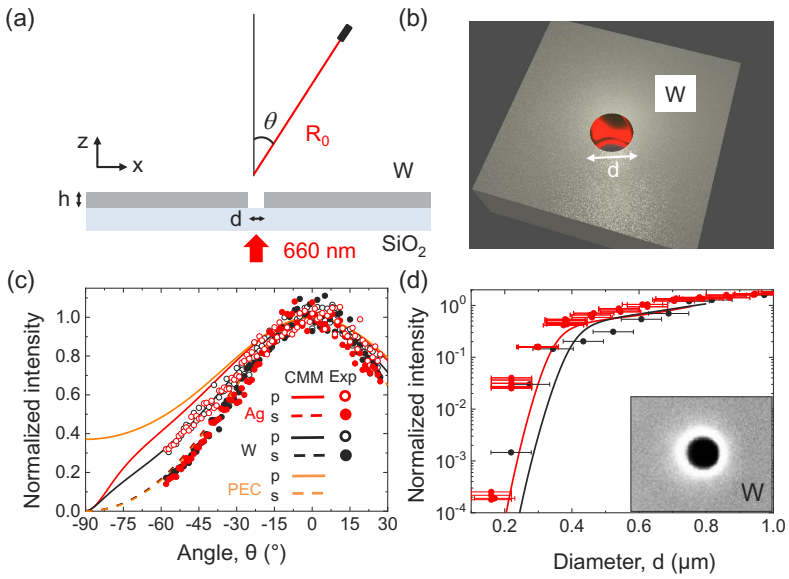

Fig. 1. (a) Schematic drawing of the experimental setup. The hole is illuminated by a cw-laser at 660 nm. Our homemade goniometer is located at a given plane forming an angle θ with the vertical direction. (b) Artistic view of a subwavelength hole pierced in an opaque W film. (c) Angular diffraction patterns from single holes with diameter d=350 nm in 400 nm thick W and Ag films illuminated at normal incidence, as a function of the incident polarization. Diffraction patterns are normalized by the intensity measured at direct transmission ($\theta = 0$). (d) Normalized-to-hole-area transmitted intensity at $\theta = 0$ for holes milled in Ag and W films as a function of the diameter (intensity is independent of polarization at $\theta = 0$). In both (c) and (d), experimental values (symbols) are compared with CMM calculations (lines) for a real metal and a PEC. In the CMM model, it is assumed that only the fundamental TE_{11} is excited in the hole, Supplement 1, Sec. 2.A. Notice that, at s-polarization, calculated values for a real metal are practically indistinguishable from those for a PEC. Inset: SEM image of a 220 nm single hole in a W film.

practically independent of the dielectric constant (theoretical curves for Ag, W, and a PEC are indistinguishable), the *p*-polarized angular spectrum in Ag is reduced to zero close to grazing radiation, in contrast with the finite values achieved for a PEC. This behavior can be explained by a reduction of the density of states radiated to the far field at large angles in order to accommodate the surface waves excited by the hole, which propagate along the metal surface [41] , see the comparison of the respective analytical expressions for a real metal and a PEC in Supplement 1, Sec. 2.A. The fact that radiation patterns in W are similar to those in Ag is thus an indirect confirmation of the existence of surface waves at the W/air interface.

The understanding of the characteristics and the role played by surface waves in the global scattering process of these antennas can be pushed a step further by using a different detection scheme. Leakage radiation microscopy (LRM) is a far-field approach based on an coherent interaction phenomenon where a thin film (60 nm) is needed to allow the leaking and the out-coupling of light in the glass substrate [49]. The latter interferes in the far field with the direct transmitted light, so that surfaces waves excited at the illuminated (air) side of the metal film are finally detected at the far field of the rear (glass) side. The optical experimental configuration for such measurements is described in Fig. 2(a). This microscopy makes it possible the imaging of both the direct (DP) and the Fourier plane (FP), and therefore provides the wavevector (k_{sw}) distribution at the output of any apertured antenna. In order to prevent fast oxidation

Optics EXPRESS

of the reference thin plasmonic Ag film, we opted for gold. Although the propagation length (L_{sw} = Im[k_{sw}]$^{-1}$) and the related dissipation are different from Ag, the intrinsic mechanism of SP excitation remains the same. To compensate the higher dissipation in gold, we used an excitation at λ=785 nm in order to increase L_{sw} up to 90 μm at the air/metal interface, closer to the value of L_{sw} = 63 μm of Ag at λ=660 nm. The LRM images in FP and DP of single slits (200 nm wide with long axis along y axis) in W and Au 60-nm films are presented in Figs. 2(b) and (c), respectively. The images in both planes show the presence of propagating surface waves launched along x. Focusing on the FP (k-space shown in Fig. 2(b)) on Au, a well-known Fano-like peak attributed to SPs is observed at the normalized free-space wavenumber q=1.02, above the dip at the critical angle in air for q=1, where $q = k_x/k_\lambda$ and $k_\lambda = 2\pi/\lambda$. Such details are better resolved in the crosscuts shown in Fig. 2(d). On the other hand, only the dip at $q = 1$ is observed for W. These experimental data in k-space can be reproduced with a fairly good agreement by a Fano-like analytical expression for the intensity in reciprocal space [49], see Supplement 1 Sec. 1.B for further details.

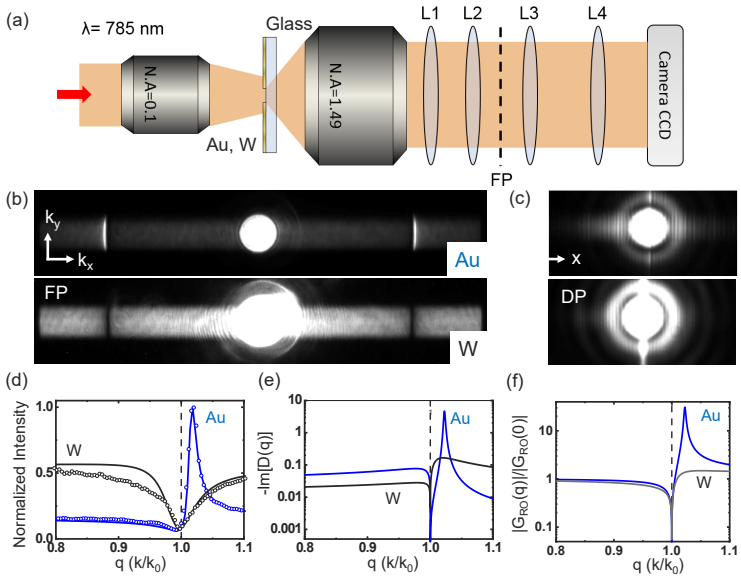

Fig. 2. (a) Schematic drawing of our homemade leakage microscope in which a cw-laser at 785 nm is used for illumination. (b),(c) Leakage radiation images of single 200-nm-wide slits in (b) reciprocal space (i.e., Fourier plane (FP)) and (c) direct plane (DP). (d) Experimental cross sections along x-direction in k-space of the two images in (b) for Au (blue circles) and W (black circles) films around q=1. Intensities are normalized by the measured value at $q = 0$. Data is fitted to a Fano-like model (solid lines, see Supplement 1, Sec. 1.B). (e) The angular EM-LDOS, -Im[$D(q)$], computed at the input side of the slit for a p-polarized incident light, as a function of the normalized wavevector q in Au and W films. (f) The absolute value of the ray-optics term of the propagator, $|G_{ro}(q)|$, normalized to its value at $q = 0$, for both materials.

Crosscuts shown in Fig. 2(d) actually provide the total angular spectrum of the subwavelength apertured antenna. It can be qualitatively compared to the ray-optics contribution of the asymptotic expansion of the propagator, G_{ro}, computed along the steepest descent path, which has been identified as responsible for the leakage radiation in LRM experiments [50]. G_{ro} is the propagator that accounts for the magnetic field produced by an the electric field of the infinitesimal single

Optics EXPRESS

slit. An analytical simple expression for G_{ro} has been reported in [19],

$$G_{ro}(r,q) = \sqrt{2\pi r^{-1}}e^{ik_\lambda - i\pi/4}q_z D(q), \tag{1}$$

where $D(q) = (2\pi)^{-1}Z_m/(q_z + Z_m)$, $Z_m = q_{z_m}/\epsilon_m$, $q_z = \sqrt{1-q^2}$, $q_{z_m} = \sqrt{\epsilon_m - q^2}$, ϵ_m the dielectric function of the metal, and r is the distance from the slit to the detection point. $G_{ro}(r.q)$ is computed at the input side of the slit. Thus, q is the free-space wavenumber. The imaginary part of $D(q)$, -Im[$D(q)$], gives the angular electromagnetic linear density of states (EM-LDOS). A detailed description of the mathematical behavior of $D(q)$ can be found in Supplement 1, Sec. 4.

Figures 2 displays (e) -Im[$D(q)$] and (f) the absolute value of $G_{ro}(q)$ for both metals as a function of q. Both quantities show similar features to those measured at the FP in Fig. 2(d). In particular, the EM-LDOS rigorously vanishes at $q = 1$ because $D(q = 1)$ is a real quantity independent of the material: $D(q = 1) = (2\pi)^{-1}$. $G_{ro}(q)$ also decreases to zero at $q = 1$ for it is proportional to q_z, which vanishes at this point. Notice that scattered and direct transmitted waves interfere at the microscope, while only the scattered field is considered in G_{ro}. It explains the differences observed in the normalized values of Figs. 2(d) and (f).

In the case of gold, the narrow peak observed in the experimental angular profile of Fig. 2(d) is reproduced by both quantities, -Im[$D(q)$] and $|G_{ro}(q)|$. This peak is centered at the real part of the normalized surface-plasmon wave vector, $q = \sqrt{\epsilon_1/(\epsilon_1 + 1)} = 1.02$ at $\lambda = 785$ nm, where ϵ_1 is the real part of the dielectric constant of Au. A broader peak with a lower intensity is developed in the W film. This peak is not centered, however, at the real part of the Zenneck wavevector ($q = 0.996$ at $\lambda = 785$ nm) but at a values of q larger than 1. This point is equal to $q \approx \sqrt{1 + (2\epsilon_2)^{-1}} = 1.01$, where $\epsilon_2 = 24$ is the large imaginary part of the dielectric constant of W, see the mathematical derivation of this expression in Supplement 1, Sec. 4. We can associate this peak with surface waves fringes observed in Fig. 2(c). Unfortunately, the wavelength of such waves cannot be quantified from the experimental results of that figure.

3. Interference of surface waves

3.1. Hole-groove antenna

Dipolar apertured antennae described in previous section display a broad emission in the far field resulting in a very limited directivity control [41,51]. A different kind of antenna, made of a single shallow concentric groove with a radius a_1, milled around a central hole, offers a better control of the far-field emission. While the study of single subwavelength holes has indirectly revealed the signature of a SW on W, the hole-groove geometry is complementary since light collected by the detector depends on the stationary SW pattern established at the metal surface. The hole performs a dual role of source of secondary light and probe for SW since it, first, excites both radiative modes that propagate to the far field and SW at the metal surface and contribute later to build the stationary pattern. In fact, SW excited by the hole are scattered several times along the metal surface by each point of both hole and groove until the complex stationary pattern of SW is finally established. Furthermore, both hole and groove openings are re-illuminated by the scattered light, modifying in this way their radiated fields, which finally interference at the far field.

Measured interference patterns from both W and Ag films in Fig. 3(a) show a multilobe signature over the whole angular range, with the position of the interference peaks varying significantly as a function of the groove radius a_1. These structured patterns evidence a coherent interaction in the far field. Focusing on the transmission intensity along the optical axis $I(0°)/I_{SH}(0°)$, which is normalized to the single hole transmission intensity, one can observe in Fig. 3(b) periodical oscillations as the radius a_1 is increased. These fringes in Figs. 3(a) and (b) show the constructive or destructive interference between fields radiated by the hole and the groove, evidencing the existence of SW on both metal films. The position of corresponding local

Optics EXPRESS

maxima and minima are close for both systems, meaning that only a minute phase difference exists between SW in both metals. In coherence with the observation done on the single dipolar apertured antenna, the recorded intensity I(0°) is much stronger for Ag films than for W films.

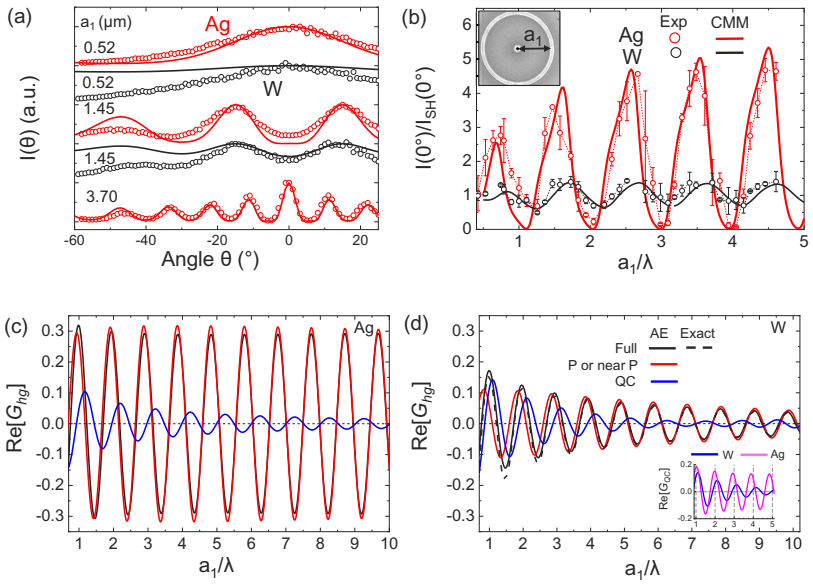

Fig. 3. Diffraction patterns (a) and transmission intensity at θ=0° (b) from single holes (d=300 nm) surrounded by a single annular groove with varying radius a_1 on the output side in W and Ag films for p-polarized illumination (incident electric field polarized along the x axis). The diffraction angular pattern is measured scanning in the xz plane. Transmission intensities are normalized with respect to $I_{SH}(0°)$ from the corresponding single holes. Groove width is set to w=200 nm and groove depth is h=80 nm, $a_1 = (r_a + r_b)/2$, where r_a (r_b) is the inner (outer) groove radius. Points represent experimental data and solid curves are calculated with Eq. (2). Re[G_{hg}] for the standard (Eq. (4)) asymptotic expansion (AE) in Ag (c) and the alternative expansion (Eq. (8)) in W (b) as a function of a_1. The exact numerical solution of Re[G_{hg}] (dashed black lines) is compared with its full AE (solid black line), as well as its constitutive asymptotic terms related to the pole (P or near P, red line), i.e., at the pole, G_p, for Ag and near the pole, $G_p/2$, for W, and quasi-cylindrical waves (QC, blue line). The inset in (d) compares G_{QC} for W and Ag (magenta line). The hole-groove distance a_1 is normalized by λ.

The normalized intensity can be cast in a simple analytical form, within the framework of the CMM approach, by improving the model presented in Ref. [41], see the derivation in Supplement 1 Sec. 2.B,

$$\frac{I(\theta,\delta)}{I_{SH}(\theta,\delta)} = \left|\frac{E'_h}{E'_0} + \frac{E'_g}{E'_0}\frac{X_{\delta g}(\theta)}{X_{\delta h}(\theta)}\right|^2, \tag{2}$$

where $\delta = p, s$ labels the polarization. E'_h and E'_g are field amplitudes of the fundamental waveguide mode at the output side of the hole and the groove, respectively. These quantities are independent of the radiated field (in particular, of θ), are function of geometrical and material parameters only, and quantify the scattering mechanisms inside the hole, the groove and along the horizontal metal surfaces. Such mechanisms have been quantitatively described above, see Supplement 1 Sec. 2.B for a complete description. Both E'_h and E'_g are normalized by the amplitude of a single (isolated) hole, E'_0. The $X_{\delta i}(\theta)$ function in Eq. (2) is equal to the overlap

Optics EXPRESS

of the fundamental mode in either the hole ($i = h$) or the groove ($i = g$) with the δ-polarized radiation modes. $X_{\delta i}(\theta)$ accounts for the far-field radiation as a function of θ.

Equation (2) is compared with experimental results in Fig. 3. Figure 3(b) shows a nice agreement between experiment and theory for the normalized intensity of both Ag and W at $\theta = 0$ as a function of a_1. Notice that $I(0,p)/I_{SH}(0,p) = I(0,s)/I_{SH}(0,s) \equiv I(0)/I_{SH}(0)$. However, the model fails to predicts the right decay of $I(\theta,p)$ as a function of θ for the lossy W in Fig. 3(a), probably due to sample imperfections.

Figure 3(b) shows that $I(0)$ oscillates as a function a_1, with a periodicity equal to the SP wavelength in Au and the Zenneck wavelength in W. While the response of plasmonic nanostructures is well known, a deep analysis of the behavior of nanostructured non-plasmonic metals is lacking in the literature. This behavior is explained here with help of a systematic asymptotic analysis of the propagators appearing in the analytical expression for the modal amplitudes E'_h (Supplement 1, Eq. S3) and E'_g (Supplement 1, Eq. S4). Both E'_h and E'_g are functions of the hole-groove, G_{hg}, and groove-groove, G_{gg}, propagators, defined by Supplement 1, Eq. S5. We shall confirm that oscillations of G_{hg} and G_{gg} are determined by SP or Zenneck-like waves at moderate distances up to the order of the propagation length L_{sw}.

The following asymptotic analysis of the propagators is based on the saddle-point technique that consists of deforming the integration path into a steepest-descent path (SDP). From the several alternative ways of making explicit the contribution of surface modes within this framework [43], we followed the specific procedure of Refs. [19,21] for it takes into account that poles and branch points along the integration path are close to the saddle point, providing an efficient way for evaluating the relative contribution of different surface waves at metal/dielectric interfaces. This procedure is well suited for both plasmonic and non-plasmonic metals [19,21]. However, it becomes cumbersome when one tries to identify, among the different asymptotic terms, a leading contribution that explains the oscillatory behavior of W. Therefore, the procedure will be improved in order to find a more convenient representation for W. We shall analyze here the asymptotic expansion of the hole-groove propagator, G_{hg}. It accounts for the stationary surface waves that are built on the metal surface in between the hole and the groove when surface waves excited by the hole are reflected by the concentric groove. Therefore, the resulting wave pattern largely differs from the cylindrical waves radiated by a single tiny hole [21]. Only the p polarization will be considered for its contribution is larger than the one for s modes. The equivalent analysis of the self-propagator G_{gg} is omitted for we arrive to conclusions that are similar to those obtained for G_{hg}.

Using the asymptotic form of the Bessel functions for large arguments and following the procedure of Refs. [19,21], the propagator can be written as the difference of two integrals, $G_{hg} = \mathcal{I}(r_b) - \mathcal{I}(r_a)$, where

$$\mathcal{I}(r) = \int_{-\infty}^{\infty} \frac{F(qk_\lambda r)e^{iqk_\lambda r}}{\sqrt{1-q^2}+z'_s}dq, \tag{3}$$

$F(x) = e^{-3i\pi/4}k_\lambda X_{ph}(qk_\lambda R)[(r_b^2/r_a^2 - 1)\,x]^{-1/2}$, R is the central hole radius, and r_a and r_b are the inner and outer radii of the groove, respectively. Retaining the first two terms in the asymptotic expansion, the integral $\mathcal{I}$ can be written as the sum of three terms,

$$\mathcal{I} = \mathcal{I}_p + \mathcal{I}_N + \mathcal{I}_{sdp}, \tag{4}$$

which are derived in Supplement 1, Sec. 3. The first term,

$$\mathcal{I}_p(r) = 2\pi i C_p(q_p k_\lambda r)e^{iq_p k_\lambda r}, \tag{5}$$

is the contribution of the residue at the pole. $\mathcal{I}_p$ represents a SP wave for Ag and a Zenneck wave for W. However, the Zenneck pole of W is in the lower Riemann sheet of the complex s plane (the pole is improper) and thus it is not crossed when the initial integration path is deformed into

Optics EXPRESS

the SDP. Hence, $\mathcal{I}_p$ does not contribute to Eq. (4) and $\mathcal{I} = \mathcal{I}_N + \mathcal{I}_{sdp}$ for W [3]. The second term, $\mathcal{I}_N$, is known as a Norton wave due to the mathematical analogy with radio waves excited by point dipoles in lossy dielectric interfaces [21]. $\mathcal{I}_N$ results from the contribution to the integral of the kink at the branch point $q = 1$ [19]. It has a marginal contribution at the values of a_1 smaller than L_{sw} that are considered in the paper and becomes relevant only at distances of several L_{sw} [19,21]. Asymptotic terms for large hole-groove distances are shown in Supplement 1, Fig. S3. On the other hand, the last term $\mathcal{I}_{sdp}$ accounts for the contribution of the remaining points of the SDP. A comprehensive description of the whole mathematical procedure is given in Ref. [43].

The asymptotic expansion is a reliable mathematical representation of the propagators at the measured distances. Figures 3 shows a very good agreement between the exact Re[G_{hg}] (black dashed line) and its asymptotic expansion (black solid line) for both (c) Ag and (d) W. G_{hg} of Ag is accurately described in Fig. 3(c) by the pole contribution G_p. The sum of the remaining asymptotic terms $G_{QC} = G_N + G_{sdp}$ provides a small contribution to the total hole-groove propagator G_{hg} in this metal.

For W, however, G_{sdp} (6) becomes the leading contribution to the asymptotic representation since the pole is not crossed and G_p does not contribute to Eq. (4). A deeper analysis of $\mathcal{I}_{sdp}$ is therefore needed. This quantity is defined as the sum of two terms, $\mathcal{I}_{sdp} = \mathcal{I}_{sdp}^{res} + \mathcal{I}_{sdp}^{NR}$. where $\mathcal{I}_{sdp}^{res}$ includes the resonant part of the integrand, which diverges at the pole, and $\mathcal{I}_{sdp}^{NR}$ accounts for the non-resonant part. Values of $\mathcal{I}_{sdp}^{NR}$, as well as those of $\mathcal{I}_N$, are small and practically equal for both metals, see Supplement 1, Fig. S3. The resonant term,

$$\mathcal{I}_{sdp}^{res}(r) = \mp\pi i C_p (q_p k_\lambda r) e^{i q_p k_\lambda r} \mathrm{erfc}(\pm i s_p \sqrt{k_\lambda r}), \tag{6}$$

is thus the leading contribution to the total propagator for W, while remains small for Ag. The real part of the argument of the complementary error function in Eq. (6) must be positive to guarantee that $\lim_{k_\lambda r \to \infty} \mathrm{erfc}(\mp i s_p \sqrt{k_\lambda r}) = 0$, where s is the integration variable in the SDP and s_p denotes its value at the pole, see Supplement 1, Sec. 3. In accordance with the values of s_p given in Supplement 1 Table S1, we must choose + and − signs for Ag and W, respectively.

We can shed light on the the behavior of $\mathcal{I}_{sdp}^{res}$ by writing the complementary error function in terms of the error function with help of the identity $\mathrm{erfc}(\pm z) = 1 \mp \mathrm{erf}(z)$ (see Supplement 1, Sec. 3),

$$\mathcal{I}_{spd}^{res} = \pi i C_p (q_p k_\lambda r) e^{i q_p k_\lambda r} \mathrm{erf}(i s_p \sqrt{k_\lambda r}) \mp \pi i C_p (q_p k_\lambda r) e^{i q_p k_\lambda r}. \tag{7}$$

The second term of the resulting expression is a surface wave with half the amplitude of the surface wave $\mathcal{I}_p$ (Eq. (5)) excited at the pole. It suggests that the presence of the nearby pole can be perceived along the SDP even when the pole is not crossed, as is the case for W. On the other hand, it can be easily shown that the first term in Eq. (7) oscillates with the free-space wavelength (see Supplement 1, Sec. 3.B), like both Norton [19,21] and quasi-cylindrical (QC) waves [16–18,23]. Therefore, $\mathcal{I}_{spd}^{res}$ may be written as the sum of a surface wave $\mathcal{I}_p/2$ and a plane wave with algebraic amplitude (given in Supplement 1, Sec. 3.B).

Minus and plus signs in Eq. (7) corresponds to Ag and W, respectively, making the resonant term in Ag smaller than in W. The plus sign for W explains the leading contribution of $\mathcal{I}_{spd}^{res}$ to the total $\mathcal{I}$. Therefore, we can employ the alternative representation,

$$\mathcal{I}' = \frac{\mathcal{I}_p}{2} + \mathcal{I}_N + \mathcal{I}'_{sdp}, \tag{8}$$

where $\mathcal{I}'_{sdp} = \mathcal{I}'^{res}_{sdp} + \mathcal{I}^{NR}_{sdp}$ and $\mathcal{I}'^{res}_{sdp} = \mathcal{I}_p \mathrm{erf}(i s_p \sqrt{k_\lambda r})/2$. Equation (8) is particularly suitable for W. Figure 3(d) shows the asymptotic propagators for the new representation (long distances of several L_{sw} are depicted in Supplement 1, Fig. S3). We find thus that $G_p/2$ is a good approximation of the full propagator at the W surface. It implies that fields on the W surface have

Optics EXPRESS

half the amplitude of those in Ag due to the fundamental nature of SW in the non-plasmonic metal and independently of losses (that mainly determine the decay length of the SW). The sum of the remaining terms, $G'_{QC} = G_N + G'_{sdp}$ that oscillates with spatial periodicity equal to λ as both G_N and G'_{sdp} do, represents a small contribution to G_{hg}.

We can see in the inset of Fig. 3(d) that the asymptotic terms G_{QC} and G'_{QC} for Ag and W, respectively, show a similar behavior: the two functions oscillate with a periodicity of about the free-space wavelength (though with a small phase difference) and decay faster than G_p. The difference between the two functions is related to material parameters. The agreement is better at short distances, for which these functions are expected to be less sensible to the metal impedance. These all are known features of the so-called quasi-cylindrical waves [16–18,23]. Therefore, we can formally state that G_{QC} and G'_{QC} represent the QC contribution in our asymptotic representation of the propagator, see Supplement 1 Sec. 3.A for a further discussion. We can estimate from Fig. 3 the relative contribution of QC, SP and Zenneck waves to the total propagator at the moderate values of a_1 considered in the paper. Interestingly, since the spatial periodicity of G'_{QC} is strictly equal to λ, W becomes and ideal material for investigating the fundamental nature of QC waves beyond the few experimental studies available in the literature, see [17,23] and references therein. Moreover, the smaller propagation length of SW in W ($L_{sw} = 5.9\ \mu$m) with respect to this in Ag ($L_{sw} = 63\ \mu$m, see Supplement 1, Table S1) concomitant with a shorter crossover distance between Zenneck-like and Norton waves (2.1 L_{sw} in W vs. 9.6 L_{sw} in Ag), as well as a higher intensity of such waves in W at the crossover point (c.f. Supplement 1 Fig. S3(a) for Ag with (d) for W), makes W an good candidate for the detection of Norton waves.

As a cautionary remark, we should stress that G_{QC} and G'_{QC} are just mathematical representations of QC waves that are only valid for the moderate values of a_1 employed in the paper. These asymptotic representations cannot be extrapolated to values of a_1 much smaller than the wavelength (for which QC are rigorously defined) at which our mathematical approach is not longer valid. This limiting case deserves a further analysis (see [26], for instance) that is beyond the scope of the present work.

3.2. Bull's eye structure

We have shown in the previous section that SW can be used to tailor the far-field emission of an apertured antenna. A system of particular interest that offers more degrees of freedom is the bull's eye antenna, which is characterized by a set of concentric grooves milled around a subwavelength hole in an opaque film (see Fig. 4). This singular geometry has turned out to be efficient for beaming the light in the far field [11,51,52], but also for generating light with high-order angular momentum by breaking the symmetry of the antenna [53].

Figure 4(b) shows the position of the peaks in the far-field diffraction patterns from W bull's eyes (n=10) as a function of the periodicity of the grooves (P) for p-polarization. The data display the same trend as already observed for BE on Ag, which corresponds to the evolution of the first order diffraction peaks, as predicted by the grating law [51]. The multilobe pattern emerging from a W antenna can thus be tuned by changing the geometrical parameters as it is done with a plasmonic Ag antenna. Two examples are presented in Figs. 4(c) and (d) for P=620 and 570 nm. In the first case, which is the resonant situation for SW, the position of the main lobes in W and Ag BE can be perfectly superimposed. In the second graph, the patterns are also quite similar, although a slight mismatch is observed. The distinct SW wave vectors in the two metals produce this difference, that results in a different interference landscape in the far field. These diffraction patterns reveals that the additional amount of light that is injected into the main lobes with respect to secondary lobes is greater in a Ag BE than in a W one. This effect can be quantified by the estimation of the directivity D of the antenna, which gives the ability of the antenna to radiate the

Optics EXPRESS

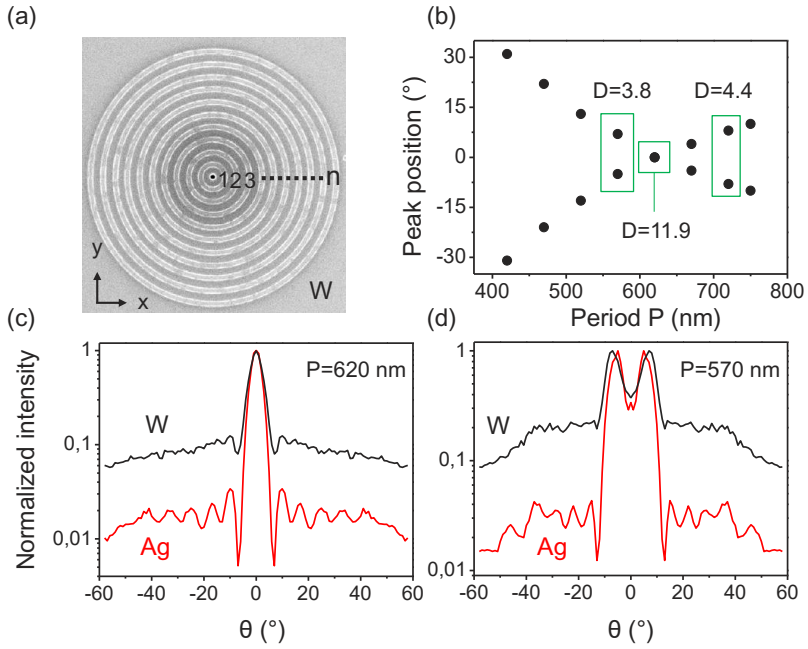

Fig. 4. (a) SEM image of a BE antenna FIB-milled on a W film. The central hole has a diameter d=300 nm and all the ten grooves have width w=200 nm and depth h=80 nm. (b) Angular peak positions (1^{rst} order) as a function of P. The directivity D is given for three different periods. (c),(d) Experimental normalized diffraction patterns at (c) P=620 nm and (d) P=570 nm under parallel p polarization for a W (black curve) and a Ag (red curve) supporting film.

EM field in specific region of space. D is defined as follows,

$$D = \frac{P_{max}(\theta,\varphi)}{P_{avg}(\theta,\varphi)} \propto \frac{I_{max}(\theta,\varphi)}{I_{avg}(\theta,\varphi)}, \tag{9}$$

where P_{avg} is the emitted power averaged over a [-60°:60°] angular sector, and φ is the azimuthal angle lying in the xy plane. Here, φ is fixed at 0° along the x-axis. The directivity of three different configurations are shown in Fig. 4(b). Similarly to Ag, the BE antenna on W is also more efficient at resonance (P=620 nm for λ=660 nm, see Supplement 1, Sec. 1.C). A directivity D=11.9 is measured on W, while D=20 was reported for Ag [51], with a peak intensity 5 times stronger than the intensity of a corresponding single apertured antenna. This difference can be attributed to the shorter propagation length of SW on W, L_{sw}=5.9 μm, compared to this on Ag (63 μm), meaning that the W SW hardly probes the furthest antenna reflectors (the last grooves of the BE). For out-of-resonance P=570 and P=710 nm, each diffraction pattern displays two off-axis symmetric lobes with respective directivities D=3.8 and 4.4 (D=7.7 and 4.1 for Ag). All these experimental observations show that BE antennas in W films have the ability to steer efficiently the beaming direction in 3D free space by tuning the geometric parameters.

4. Conclusion

To conclude, we have demonstrated, both experimentally and theoretically, that surface waves generated at the output of apertured antennas on non-plasmonic W films can be used to tailor the far-field emission. The polarization-dependent diffraction patterns and the leakage signal

Optics EXPRESS

emerging from simple and complex apertured antennas in both kinds of metal have been recorded and analyzed. The systematic comparison with plasmonic metals, either Ag or Au, allowed us to stress the propagation and damping properties of the SWs at work on these nanostructures. From our measurement, we attributed them a Zenneck-like behavior at optical frequencies that matches our observations.

We have developed an asymptotic expansion that evaluates the relative contribution of surface waves in the radiation pattern. We found that, although single Zenneck waves are not excited at the surface of W (as its improper pole is located in the lower Riemann sheet of the complex plane) a weaker Zenneck wave excitation is still perceived by the system due to the proximity of the pole to the integration path. This excitation oscillates with the wavelength of the Zenneck wave but it has one-half of its amplitude. This reduced amplitude is a fundamental property of Zenneck waves not related to their inherent losses. Other terms of the asymptotic expansion behave as a single wave that propagates with free-space wavelength (equivalent waves in Ag are material dependent) and can be related to a mathematical representation of quasi-cylindrical waves. When the hole-groove distance becomes larger than the propagation length, Norton waves are excited in W at distances much smaller than in Ag and with a higher intensity. Such features makes W a good candidate for fundamental studies of quasi-cylindrical and Norton waves.

We hope that the present work motivate further experimental and theoretical studies on the fundamental properties of non-plasmonic materials opening up new research avenues and possible applications beyond SP-based NanoOptics.

Funding. University of Strasbourg Institute for Advanced Study (USIAS) (ANR-10-IDEX- 0002-02); SFRI STRATUS (ANR-20-SFRI-0012); IdEx Unistra (ANR-10-IDEX- 0002); Spanish Ministry of Science, Innovation and Universities - State Research Agency (MAT2017-88358-C3-2-R); Ministerio de Ciencia e Innovación/Agencia Estatal de Investigación (MICINN/AEI) (PID2020-115221GB-C41); National Natural Science Foundation of China (62174175); LabEx Chimie des Systèmes Complexes (ANR-10-LABX- 0026-CSC); Laboratoires d'excellence Nanostructures en Interaction avec leur Environnement (ANR-11-LABX-0058-NIE).

Acknowledgments. This work is part of the Interdisciplinary Thematic InstituteQMat of the University of Strasbourg, CNRS and Inserm. It was supported by the following programs: IdEx Unistra (ANR-10-IDEX- 0002), SFRI STRATUS project (ANR-20-SFRI-0012), the Labex CSC project ANR-10-LABX-0026-CSC, the Labex NIE project ANR-11-LABX-0058-NIE, and USIAS (ANR-10-IDEX- 0002-02), under the framework of the French Investments for the Future Program. J.Y. acknowledges the support of the Natural Science Foundation of China (Grant No.62174175). L.M.M. acknowledges Project PID2020-115221GB-C41 financed by MCIN/AEI/10.13039/501100011033. F.d.L.P. acknowledges financial support from Spanish Ministry of Science, Innovation and Universities - State Research Agency through project MAT2017-88358-C3-2-R. L.M.M. and F.d.L.P. acknowledge the Aragon Government through Project Q-MAD.

Disclosures. The authors declare no conflicts of interest.

Data availability. Data underlying the results presented in this paper are not publicly available at this time but may be obtained from the authors upon reasonable request.

Supplemental document. See Supplement 1 for supporting content.

References

1. J. Zenneck, "Über die fortpflanzung ebener elektromagnetischer wellen mngs einer ebenen leiterflache und ihre beziehung zur drahtlosen telegraphie," Ann. Phys. **328**(10), 846–866 (1907).
2. A. Sommerfeld, "Über die ausbreltung der wellen in der drahtlosen telegraphie," Ann. Phys. **28**, 665-736 (1909).
3. J. R. Wait, "The ancient and modern history of em ground-wave propagation," IEEE Antennas Propag. Mag. **40**(5), 7–24 (1998).
4. R. Collin, "Hertzian dipole radiating over a lossy earth or sea: Some early and late 20th-century controversies," IEEE Antennas Propag. Mag. **46**(2), 64–79 (2004).
5. K. A. Michalski and J. R. Mosig, "The sommerfeld half-space problem revisited: from radio frequencies and zenneck waves to visible light and fano modes," J. Electromagn. Waves Appl. **30**(1), 1–42 (2015).
6. C. Genet and T. Ebbesen, "Light in tiny holes," Nature **445**(7123), 39–46 (2007).
7. S. Nie and S. Emery, "Probing single molecules and single nanoparticles by surface-enhanced raman scattering," Science **275**(5303), 1102–1106 (1997).
8. K. Kneipp, Y. Wang, H. Kneipp, L. Perelman, I. Itzkan, R. Dasari, and M. Feld, "Single molecule detection using surface-enhanced raman scattering (SERS)," Phys. Rev. Lett. **78**(9), 1667–1670 (1997).

Optics EXPRESS

9. T. Ebbesen, H. Lezec, H. Ghaemi, T. Thio, and P. Wolff, "Extraordinary optical transmission through sub-wavelength hole arrays," Nature **391**(6668), 667–669 (1998).
10. F. J. García-Vidal, L. Martín-Moreno, T. W. Ebbesen, and L. Kuiper, "Light passing through subwavelength apertures," Rev. Mod. Phys. **82**(1), 729–787 (2010).
11. H. Lezec, A. Degiron, E. Devaux, R. Linke, L. Martin-Moreno, F. Garcia-Vidal, and T. Ebbesen, "Beaming light from a subwavelength aperture," Science **297**(5582), 820–822 (2002).
12. M. Noginov, G. Zhu, A. Belgrave, R. Bakker, V. Shalaev, E. Narimanov, S. Stout, E. Herz, T. Suteewong, and U. Wiesner, "Demonstration of a spaser-based nanolaser," Nature **460**(7259), 1110–1112 (2009).
13. R. Oulton, V. Sorger, T. Zentgraf, R. Ma, C. Gladden, L. Dai, G. Bartal, and X. Zhang, "Plasmon lasers at deep subwavelength scale," Nature **461**(7264), 629–632 (2009).
14. A. Cuche, O. Mahboub, E. Devaux, C. Genet, and T. Ebbesen, "Plasmonic coherent drive of an optical trap," Phys. Rev. Lett. **108**(2), 026801 (2012).
15. M. Juan, M. Righini, and R. Quidant, "Plasmon nano-optical tweezers," Nat. Photonics **5**(6), 349–356 (2011).
16. P. Lalanne and J. Hugonin, "Interaction between optical nano-objects at metallo-dielectric interfaces," Nat. Phys. **2**(8), 551–556 (2006).
17. L. Aigouy, P. Lalanne, J. Hugonin, G. Julié, V. Mathet, and M. Mortier, "Near-field analysis of surfacewaves launched at nanoslit apertures," Phys. Rev. Lett. **98**(15), 153902 (2007).
18. H. Liu and P. Lalanne, "Microscopic theory of the extraordinary optical transmission," Nature **452**(7188), 728–731 (2008).
19. A. Nikitin, S. Rodrigo, F. Garcia-Vidal, and L. Martin-Moreno, "In the diffraction shadow: Norton waves versus surface plasmon polaritons in the optical region," New J. Phys. **11**(12), 123020 (2009).
20. W. Dai and C. M. Soukoulis, "Theoretical analysis of the surface wave along a metal-dielectric interface," Phys. Rev. B **80**(15), 155407 (2009).
21. A. Nikitin, F. Garcia-Vidal, and L. Martin-Moreno, "Surface electromagnetic field radiated by a subwavelength hole in a metal film," Phys. Rev. Lett. **105**(7), 073902 (2010).
22. J. Q. A. Sihvola and I. Lindell, "Bridging the gap between plasmonics and zenneck waves," IEEE Antennas Propag. Mag. **52**(1), 124–136 (2010).
23. F. van Beijnum, C. Rétif, C. Smiet, H. Liu, P. Lalanne, and M. P. van Exter, "Quasi-cylindrical wave contribution in experiments on extraordinary optical transmission," Nature **492**(7429), 411–414 (2012).
24. M. Faryad and A. Lakhtakia, "Grating-coupled excitation of the Uller-Zenneck surface wave in the optical regime," J. Opt. Soc. Am. B **31**(7), 1706–1711 (2014).
25. V. E. Babicheva, S. Gamage, L. Zhen, S. B. Cronin, V. S. Yakovlev, and Y. Abate, "Near-field surface waves in few-layer mos2," ACS Photonics **5**(6), 2106–2112 (2018).
26. F. López-Tejeira, F. J. García-Vidal, and L. Martín-Moreno, "Scattering of surface plasmons by one-dimensional periodic nanoindented surfaces," Phys. Rev. B **72**(16), 161405 (2005).
27. M. Sarrazin and J.-P. Vigneron, "Optical properties of tungsten thin films perforated with a bidimensional array of subwavelength holes," Phys. Rev. E **68**(1), 016603 (2003).
28. H. Lezec and T. Thio, "Diffracted evanescent wave model for enhanced and suppressed optical transmission through subwavelength hole arrays," Opt. Express **12**(16), 3629–3651 (2004).
29. F. Przybilla, A. Degiron, J. Laluet, C. Genet, and T. Ebbesen, "Optical transmission in perforated noble and transition metal films," J. Opt. A: Pure Appl. Opt. **8**(5), 458–463 (2006).
30. S. Rodrigo, F. Garcia-Vidal, and L. Martin-Moreno, "Influence of material properties on extraordinary optical transmission through hole arrays," Phys. Rev. B **77**(7), 075401 (2008).
31. J. A. Schuller, E. S. Barnard, W. Cai, Y. C. Jun, J. S. White, and M. L. Brongersma, "Plasmonics for extreme light concentration and manipulation," Nat. Mater. **9**(3), 193–204 (2010).
32. L. Novotny and N. van Hulst, "Antennas for light," Nat. Photonics **5**(2), 83–90 (2011).
33. P. Biagioni, J.-S. Huang, and B. Hecht, "Nanoantennas for visible and infrared radiation," Rep. Prog. Phys. **75**(2), 024402 (2012).
34. J. Prikulis, P. Hanarp, L. Olofsson, D. Sutherland, and M. Käll, "Optical spectroscopy of nanometric holes in thin gold films," Nano Lett. **4**(6), 1003–1007 (2004).
35. H. Shin, P. B. Catrysse, and S. Fan, "Effect of the plasmonic dispersion relation on the transmission properties of subwavelength cylindrical holes," Phys. Rev. B **72**(8), 085436 (2005).
36. F. J. G.-V. A. Y. Nikitin, D. Zueco, and L. Martín-Moreno, "Electromagnetic wave transmission through a small hole in a perfect electric conductor of finite thickness," Phys. Rev. B **78**(16), 165429 (2008).
37. A. Baudrion, F. de León-Pérez, O. Mahboub, A. Hohenau, H. Ditlbacher, F. J. García-Vidal, J. Dintinger, T. W. Ebbesen, L. Martín-Moreno, and J. R. Krenn, "Coupling efficiency of light to surface plasmon polariton for single subwavelength holes in a gold film," Opt. Express **16**(5), 3420–3429 (2008).
38. T. Coenen and A. Polman, "Optical properties of single plasmonic holes probed with local electron beam excitation," ACS Nano **7**, 7350-7358 (2014).
39. J. Jung and O. Keller, "Microscopic theory of diffraction of light from a small hole," Phys. Rev. A **90**(4), 043830 (2014).
40. J. Yang, J.-P. Hugonin, and P. Lalanne, "Near-to-far field transformations for radiative and guided waves," ACS Photonics **3**(3), 395–402 (2016).

Optics EXPRESS

41. J.-M. Yi, A. Cuche, F. de León-Pérez, A. Degiron, E. Laux, E. Devaux, C. Genet, J. Alegret, L. Martín-Moreno, and T. Ebbesen, "Diffraction regimes of single holes," Phys. Rev. Lett. **109**(2), 023901 (2012).
42. F. Mariani, F. de León-Pérez, K. J. A. Vendel, L. Martín-Moreno, and M. P. V. Exter, "Angle resolved transmission through metal hole gratings," Opt. Express **25**(8), 9061–9070 (2017).
43. L. P. Felsen and N. Marcuvitz, *Radiation and Scattering of Waves* (IEEE, 1994).
44. A. Vorobyev and C. Guo, "Femtosecond laser-induced periodic surface structure formation on tungsten," J. Appl. Phys. **104**(6), 063523 (2008).
45. A. Vorobyev, V. Makin, and C. Guo, "Brighter light sources from black metal: Significant increase in emission efficiency of incandescent light sources," Phys. Rev. Lett. **102**(23), 234301 (2009).
46. S. Thomas, M. Krueger, M. Foerster, M. Schenk, and P. Hommelhoff, "Probing of optical near-fields by electron rescattering on the 1 nm scale," Nano Lett. **13**(10), 4790–4794 (2013).
47. J. Park, S. Han, P. Nagpal, and D. Norris, "Observation of thermal beaming from tungsten and molybdenum bull's eyes," ACS Photonics **3**(3), 494–500 (2016).
48. S. Carretero-Palacios, O. Mahboub, F. García-Vidal, L. Martín-Moreno, S. Rodrigo, C. Genet, and T. Ebbesen, "Mechanisms for extraordinary optical transmission through bull's eye structures," Opt. Express **19**(11), 10429–10442 (2011).
49. B. Stein, J.-Y. Laluet, E. Devaux, C. Genet, and T. W. Ebbesen, "Fano resonances and leakage radiation for high-resolution plasmonic sensing," J. Phys. Chem. C **116**(10), 6092–6096 (2012).
50. A. Drezet and C. Genet, "Imaging surface plasmons: From leaky waves to far-field radiation," Phys. Rev. Lett. **110**(21), 213901 (2013).
51. J.-M. Yi, A. Cuche, E. Devaux, C. Genet, and T. Ebbesen, "Beaming visible light with a plasmonic aperture antenna," ACS Photonics **1**(4), 365–370 (2014).
52. C. Osorio, A. Mohtashami, and A. Koenderink, "K-space polarimetry of bullseye plasmon antennas," Sci. Rep. **5**(1), 9966 (2015).
53. Y. Gorodetski, A. Drezet, C. Genet, and T. Ebbesen, "Generating far-field orbital angular momenta from near-field optical chirality," Phys. Rev. Lett. **110**(20), 203906 (2013).